Interfacial instability of pressure-driven channel flow for a two-species model of entangled wormlike micellar solutions

Michael Cromer[a], L. Pamela Cook[a], Gareth H. McKinley[b]

[a]*Department of Mathematical Sciences, University of Delaware, Newark, DE 19716, USA*
[b]*Department of Mechanical Engineering, Massachusetts Institute of Technology, Cambridge, MA 02139, USA*

Abstract

We examine the linear stability of the one dimensional inhomogeneous (shear banded) pressure-driven flow through a rectilinear microchannel predicted by the VCM model (Vasquez et al., A network scission model for wormlike micellar solutions I: model formulation and homogeneous flow predictions. *J. Non-Newtonian Fluid Mech.* 144:122-139, 2007). The VCM model is a microstructural network model that incorporates the breakage and reforming of two elastically-active species (a long species 'A' and a shorter species 'B'). The model consists of a set of coupled nonlinear partial differential equations describing the two micellar species, which relax due to reptative and Rousian stress-relaxation mechanisms as well as breakage events. The model includes nonlocal effects arising from stress-microstructure diffusion and we investigate the effect of these nonlocal terms on the linear stability of the pressure-driven flow. Calculation of the full eigenspectrum shows that the mode of instability is a sinuous (odd) interfacial mode, in agreement with previous calculations for the shear-banded Johnson-Segalman model (Fielding and Wilson, Shear banding and interfacial instability in planar Poiseuille flow. *J. Non-Newtonian Fluid Mech.* 165:196-202, 2010). Increased diffusion, or smaller characteristic channel dimensions, smoothes the kink in the velocity profile that develops at the shear band and progressively reduces spectrum of unstable modes. For sufficiently large diffusion this

Email addresses: `cromer@math.udel.edu` (Michael Cromer), `cook@math.udel.edu` (L. Pamela Cook), `gareth@mit.edu` (Gareth H. McKinley)

smoothing effect eliminates the instability entirely and restabilizes the base (shear-banded) velocity profile.

1. Introduction

Micelles are formed by the aggregation of surfactant molecules in solution. Depending upon the surfactant concentration, ionic strength and temperature, they can form a variety of morphologies such as spheres, ellipsoids, and, of interest for this paper, long flexible cylindrical structures, commonly referred to as wormlike micelles. Above an overlap concentration, these wormlike micelles (worms) are long enough to entangle and form a physical network reminiscent of entangled polymer solutions. Consequently, wormlike micellar solutions relax through the same processes as polymers including reptation and Rouse-like segmental diffusion. In addition, thermal fluctuations result in dynamic chain rupture and reforming events, hence they are referred to as 'living polymers' [1]. These micellar solutions have many industrial uses, for instance they are used as thickeners in many consumer products and have applications as fracturing agents in enhanced oil recovery.

Experiments on wormlike micellar solutions in a cylindrical Couette device [2, 3, 4, 5] show that even in this simple flow, in which the shear stress is nominally constant across the gap, inhomogeneous features can develop. Specifically, the flow splits into two 'bands'; a region of high shear rate adjacent to the inner rotating wall connected to a low shear rate domain adjacent to the outer fixed wall. This phenomenon is commonly referred to as shear banding. Numerous studies on the modeling of shear banding in a steady flow have been reported [1, 6, 7, 8, 9] and there are comprehensive reviews on the subject in [10, 11, 12, 13].

A variety of nonlinear, viscoelastic constitutive models have been developed that can capture the shear banding phenomenon observed for wormlike micellar solutions in cylindrical Couette flow. Examples of viscoelastic constitutive models that have been used to describe banding include the Johnson-Segalman model [7], the Giesekus model [14], the Rolie-Poly model [15] and the reptation-reaction model [6]. Unfortunately, these models often fail in their ability to predict behavior of wormlike micelles in other modes of deformation. The Johnson-Segalman model predicts unphysical oscilla-

tions in step-strain [16], and an unbounded extensional viscosity in filament stretching [16]. The steady state extensional viscosity for the Giesekus model plateaus at high extension rates [16] and thus does not predict the extreme extensional thinning reported in wormlike micellar solutions [17, 18]. For these reasons we were lead to consider a two-species model developed in [8], the VCM (Vasquez, Cook, McKinley) model, to describe entangled wormlike micellar mixtures.

The VCM model is derived from transient network theory and is based upon a simplified version of the 'living polymer' model [1]. It incorporates the physics of the worms in that it includes two micellar species: a long species 'A' (of length L), which can break into two shorter species 'B', which themselves can recombine to form one 'A' chain. The breakage rate of the long entangled wormlike chains depends on the local stress and strain rate, and this, in addition to diffusive effects due to Brownian motion, and consideration of the finite length of the worms, leads to a coupling between the fluid microstructure and the global kinematics of the flow. The breakage (and hence disappearance) of the long ('A') species worms (similar to the destruction of tubes due to retraction and reptation in the reptation-reaction model [6]) is responsible for the downturn (non-monotonicity) in the steady state constitutive curve. The upturn in the constitutive curve at higher shear rates in the VCM model is due to the formation of the short ('B') species and its viscoelastic character. This is in contrast to the single species models (for example Johnson-Segalman, Giesekus) in which an unphysically large viscosity of the Newtonian solvent is introduced to describe the upturn at high shear rates. The VCM model, in addition to being able to capture shear banding in circular Taylor-Couette flow, has been studied extensively in several other flows, including large amplitude oscillatory shear (LAOS) [19], uniaxial elongational flows [20], and most recently in pressure-driven channel flow [21]. The predictions of the VCM model in these flows show excellent qualitative agreement with experimental behavior of wormlike micellar solutions. While the VCM model does succeed at describing many aspects of the physical response of wormlike micelles in these flows, one weakness is that the second normal stress difference is identically zero.

In a recent study [21], we examined the one-dimensional pressure-driven channel flow of the VCM model. The model incorporates nonlocal diffusive effects which are controlled by the magnitude of the dimensionless diffusion parameter ($\delta = \lambda D/H^2$, where D is the diffusivity of the micellar species, λ the relaxation time and H the channel height). These nonlocal effects include

3

a decrease in the interfacial shear stress for increasing δ (decreasing channel heights) similar to that seen in experiments [22]. Using singular perturbation analysis we showed that a weak boundary layer in the velocity and shear stress exists at the walls whose width depends on the diffusion parameter and the ratio of the solvent to micellar viscosity. Additionally, above a critical pressure drop, a time-evolving interior shear layer (corresponding to the onset of shear banding) develops, splitting the flow into two regions: a high shear rate region adjacent to the outer walls connected to a low shear rate flow in the center of the channel. In this paper we investigate the linear stability of these 1D, steady state solutions to infinitesimal disturbances in the flow/flow-gradient plane.

Instabilities in shear banding of wormlike micellar solutions have been observed experimentally in various shear flows. Fluctuations of the interface between the shear bands have been observed in circular Couette flow [23, 24, 25] and flow in a cone-and-plate rheometer [26]. For example, experiments in [24] showed the existence of a destabilised interface with velocity rolls in the vorticity direction. Fielding showed that, for a sufficiently small interfacial width, the Johnson-Segalman model is able to predict this shear banding instability on imposition of disturbances in the flow-gradient/vorticity plane [27]. In subsequent work she further showed that this interfacial instability in the gradient/vorticity plane in planar geometries is a result of a jump in the second normal stress difference [28]. This interfacial instability is suppressed in flows with increasing curvature, for which a bulk Taylor-Couette instability arises. The dimensionless curvature of the cell used in [24] is small, approximately 0.08, thus the appearance of an interfacial instability is in agreement with the predictions of [28]. The analysis of [28] suggests that the VCM model will not exhibit vortical instabilities in wall-driven flows due to its lack of a second normal stress difference.

In addition to interfacial instabilities arising in wall-driven flows, an interfacial instability resulting in an undulating interface has been seen in experimental measurements of the pressure-driven flow of wormlike micelles in a pipe [29] and along a planar microchannel [30]. In the latter, undulations along the interface were observed in the gradient/vorticity plane in agreement with the corresponding analysis of [28] for planar geometries. Much of the theoretical work on unstable shear banded states has been carried out using the Johnson-Segalman model. In this paper we consider for the first time stability of the VCM constitutive model.

For simplicity and tractability in the present analysis we only consider

two-dimensional (2D) disturbances in the flow/flow-gradient plane. We do not, however, assume that the VCM model obeys Squire's theorem [31]; that is, we do not assume that 2D disturbances are more unstable than three-dimensional (3D) disturbances. The validity of Squire's theorem, which was originally proved for Newtonian fluids [31], has been investigated for some viscoelastic models, namely the upper convected Maxwell, Oldroyd-B and second-order-fluid models. The upper convected Maxwell and Oldroyd-B models have been shown to satisfy Squire's theorem [32]. The application of the theorem to the second-order fluid model depends solely on the second normal stress coefficient with invalidity corresponding to a nonzero value [33]. To this end it is worthwhile to note that the second normal stress coefficient for the VCM model is zero. This is in contrast to the Giesekus model, which has a nonzero second normal stress difference and for which Squire's theorem does not apply [34]. The question of the validity of Squire's theorem for the VCM model remains open.

There is extensive literature on the linear stability of planar channel flow of both Newtonian and viscoelastic models and the viscometric properties predicted by each model play a major role in governing the stability characteristics. Several of the non-Newtonian models studied include the second-order-fluid (SOF) [35], the upper convected Maxwell (UCM) model [35, 36, 37, 38], the Oldroyd-B (OB) model [36, 37, 38], the Giesekus model [39, 34, 40], the White-Metzner (WM) model [41], the Phan-Thien Tanner (PTT) model [40] and the Johnson-Segalman (JS) model [42].

The Reynolds number ($Re = \rho H^2/(\lambda \eta_0)$ where ρ is the density, H the channel height, λ the relaxation time and η_0 the zero shear rate viscosity) scales with the square of the channel height so that for flow of entangled micellar solutions in a microchannel (corresponding experimentally to 1μm $\leq H \leq 100\mu$m), Re is negligibly small and we thus assume inertialess flow ($Re \rightarrow 0$) and consider only elastic instabilities in the present study. Under this condition, the flow of a Newtonian fluid is linearly stable (Newtonian fluids are linearly stable for pressure-driven rectilinear flow up to $Re_c = 5772.22$ [43]). No purely elastic instabilities have been found for the UCM and OB (constant viscosity) models in planar Poiseuille flow [35, 36, 38]. In recent work it has been shown that in wall-driven, plane Couette flow, the UCM model exhibits a nonlinear, elastic instability (very small Reynolds number) where the base flow is linearly stable [44]. Additionally, [37] showed that the addition of stress diffusivity to the OB model does not result in loss of stability of the inertialess channel flow; in fact, diffusion has

a stabilizing effect. Using a modified OB model, [45] showed that if there is a steep gradient in the first normal stress coefficient across the gap then a purely elastic mode of instability may occur. In order to probe other mechanisms of instability, [41] investigated a shear thinning WM model and showed that an elastic instability is possible for a sufficient amount of shear thinning (faster than $\eta \gtrsim \dot{\gamma}^{-0.7}$). In accordance with the observed shear thinning mechanism [40] found that both the Giesekus and PTT models can exhibit purely elastic instabilities (the former conclusion having not been found by previous authors [39, 34]). Because previous studies have focused on parameter choices in these models that are appropriate for the moderate levels of shear thinning observed in polymer melts they have not considered the shear banding limit of interest in entangled micellar solutions ($\eta \sim \dot{\gamma}^{-1}$). In addition these previous analyses do not include diffusion, which as shown in [21] is important in microchannel flows. The effects of shear banding and diffusion, however, were considered for a Johnson-Segalman model in the work of [42]. In that work, the authors showed that for this nonlinear viscoelastic model shear banding can be responsible for an elastic instability and the dominant mode of instability is a sinuous (odd, snake-like) mode as opposed to a varicose (even, sausage-like) mode. In their work only small diffusivity parameters were considered with values appropriate for macroscopic pipes and channels, but orders of magnitude smaller than one would expect for the flow of wormlike micelles in microchannels; however they do find a linear relation between the growth rate and diffusion and anticipate linear stability at a critical interfacial width. In the present paper we investigate the stability of a two-species, scission/reforming model, the VCM model, designed for wormlike micellar solutions and we consider the role of increasing the range of values of diffusivity consistent with microchannel flow.

Based on the previous work it is reasonable to expect that a shear banded velocity profile for the VCM model will be linearly unstable to purely elastic perturbations in the flow direction when the streamwise elastic stress becomes large enough. This is based on the facts that associated with shear banding is an extreme shear thinning (due to the shear stress plateau) of the fluid and that the VCM model predicts a steep gradient in the first normal stress difference in banded flow [21]. Thus, the goal of this work is to study the structure and characteristics of purely elastic instabilities that arise for the rectilinear pressure-driven flow of the VCM model by probing the parameter space that controls the onset of instability as well as the form of the resulting perturbed flow field (i.e. the eigenfunctions).

2. The VCM (scission/reforming) Model

2.1. Equations

The nondimensional VCM model constitutive equations are [8]

$$\mu\frac{Dn_A}{Dt} - 2\delta_A\nabla^2 n_A + \delta_A\nabla\nabla : \mathbf{A} = \frac{1}{2}c_B n_B^2 - c_A n_A \tag{1}$$

$$\mu\frac{Dn_B}{Dt} - 2\delta_B\nabla^2 n_B + 2\delta_B\nabla\nabla : \mathbf{B} = -c_B n_B^2 + 2c_A n_A \tag{2}$$

$$\mu\mathbf{A}_{(1)} + \mathbf{A} - n_A\mathbf{I} - \delta_A\nabla^2\mathbf{A} = c_B n_B\mathbf{B} - c_A\mathbf{A} \tag{3}$$

$$\epsilon\mu\mathbf{B}_{(1)} + \mathbf{B} - \frac{n_B}{2}\mathbf{I} - \epsilon\delta_B\nabla^2\mathbf{B} = \epsilon\left[-2c_B n_B\mathbf{B} + 2c_A\mathbf{A}\right] \tag{4}$$

Here n_A and n_B represent the number density of the 'A' and 'B' species respectively and $\mathbf{A}$ and $\mathbf{B}$ are the respective conformation tensors. The subscript $()_{(1)}$ denotes the upper-convected derivative and is given by:

$$\frac{\partial()}{\partial t} + \mathbf{v}\cdot\nabla() - \left((\nabla\mathbf{v})^T\cdot() + ()\cdot\nabla\mathbf{v}\right). \tag{5}$$

The reforming rate c_B of the short 'B' species is taken to remain at the (constant) equilibrium reforming rate (c_{Beq}), and the breakage rate of the long 'A' chains is enhanced by a coupling between the strength of the shear flow and the stretching of the entangled micellar chains

$$c_A = c_{Aeq} + \mu\frac{\xi}{3}(\dot{\boldsymbol{\gamma}} : \frac{\mathbf{A}}{n_A}) \tag{6}$$

where c_{Aeq} is the equilibrium breakage rate.

The constitutive equations are coupled to the inertialess flow equations of conservation of mass:

$$\nabla\cdot\mathbf{v} = \mathbf{0} \tag{7}$$

and conservation of momentum:

$$\nabla\cdot\mathbf{\Pi} + \mathbf{f} = \mathbf{0} \tag{8}$$

where $\mathbf{\Pi}$ is the total stress of the wormlike micellar solution and is given by

$$\mathbf{\Pi} = p\mathbf{I} + (n_A + n_B)\mathbf{I} - \mathbf{A} - 2\mathbf{B} - \beta\dot{\boldsymbol{\gamma}} \tag{9}$$

and $\mathbf{f}$ is the nondimensional, externally imposed driving force (pressure drop), which for 1D channel flow in the positive x direction (see Fig.2) is given by $(\mathcal{P} = \frac{\Delta P H}{G_0 L}, 0, 0)$.

The following scalings have been adopted to nondimensionalize the VCM model: the spatial dimension is scaled by the channel height H ($\mathbf{x} = \mathbf{x}'/H$); time is scaled as $t = t'/\lambda_{eff}$ where $\lambda_{eff} = \frac{\lambda_A}{1+c'_{Aeq}\lambda_A}$ is the effective relaxation time, which is reduced from the 'A' species reptation time (λ_A) due to the breakage of the long chains; velocity is scaled as $\mathbf{v} = \mathbf{v}'\lambda_{eff}/H$; and the micellar stress is scaled by the plateau modulus G_0 ($\mathbf{A}, \mathbf{B} = ()'/G_0$).

The dimensionless parameters in the equations above include the viscosity ratio $\beta = \frac{\eta_S}{\eta_0}$, two time ratios, $\mu = \frac{\lambda_A}{\lambda_{eff}}$ and $\epsilon = \frac{\lambda_B}{\lambda_A}$, a dimensionless diffusivity $\delta_A = \frac{\lambda_A D_A}{H^2}$ and a single nonlinear parameter ξ that controls the strain and rate dependence of material properties such as the damping function and shear thinning viscosity [46]. Values for these parameters, fitted to data from [47], are: $\beta = 7 \times 10^{-5}$, $\mu = 1.9$, $c_{Aeq} = 0.9$, $c_{Beq} = 1.4$, $\epsilon = 6.27 \times 10^{-4}$, $\xi = 0.3$. The relaxation times λ_A, λ_B, the equilibrium breakage and reforming rates c_{Aeq}, c_{Beq}, and thus the effective relaxation time λ_{eff} were determined from small amplitude oscillatory shear experiments (see [8]). The solvent viscosity ratio $\beta = \eta_s/(\lambda_{eff}G_0)$ is then determined using the viscosity of water. The nonlinear parameter ξ is determined by fits to step strain experiments (see [9]). In fact higher values of ξ, for example of 0.7 may be more realistic (see [9, 46]). The dimensionless diffusion parameters are then determined if D_A, D_B are known. In this work the diffusivity parameters are taken such that $\delta_A = \delta_B$ and we therefore use the simplified notation δ. Part of the goal of microchannel experiments is to determine the physically appropriate values for the magnitude of δ. The homogeneous non-monotonic constitutive curve for the VCM model using these parameters is shown in Fig.1. In full (inhomogeneous) shear flow the flow curve shows a stress plateau at shear rates corresponding to those for which banding occurs. For a small value of the diffusivity parameter ($\delta = 10^{-4}$) the macroscopic flow curve in circular Taylor-Couette flow is shown in Fig.1.

We impose a no slip boundary condition on the velocity at the solid walls

$$\mathbf{v} = 0. \tag{10}$$

The inclusion of stress diffusion necessitates the use of boundary conditions on the stress and number density. As discussed in [21], we assume no flux of
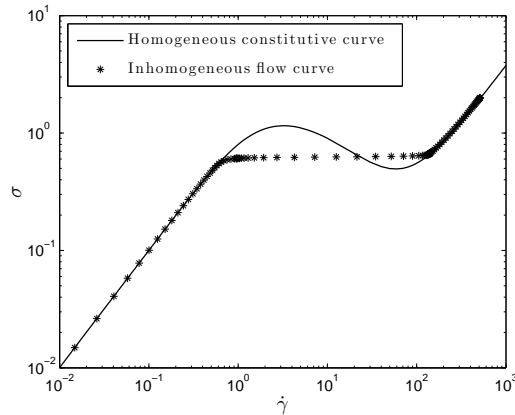
Figure 1: The homogeneous constitutive curve (solid line) for the VCM model for the values of the parameters discussed in the text. The apparent flow curve is shown by the symbols for $\delta = 10^{-4}$, in a circular Taylor-Couette cell with small curvature $p = (R_o - R_i)/R_i = 0.01$.

species across solid boundaries

$$\mathbf{n} \cdot \mathbf{j}_A = \delta_A \mathbf{n} \cdot (2\nabla n_A - \nabla \cdot \mathbf{A}) = 0 \tag{11}$$

$$\mathbf{n} \cdot \mathbf{j}_B = \delta_B \mathbf{n} \cdot (2\nabla n_B - 2\nabla \cdot \mathbf{B}) = 0 \tag{12}$$

and no flux of conformation across the solid walls

$$\mathbf{n} \cdot \nabla \mathbf{A} = 0 \tag{13}$$

$$\mathbf{n} \cdot \nabla \mathbf{B} = 0 \tag{14}$$

where $\mathbf{n}$ is the outward pointing normal to the wall. The no flux of conformation boundary condition has been suggested and used by a number of authors when analyzing models with stress diffusion [7, 48, 49] although other authors have considered Dirichlet conditions on stress [50], or the effect of mixed (Robin) boundary conditions on the stress [15].

9

3. Base state

3.1. Geometry and Equations

Fig.2 is a schematic diagram of the 2D channel flow neglecting variations in the transverse direction ($\frac{\partial}{\partial z} = 0$). For the base state it is assumed that the flow is uniform in the flow direction ($\frac{\partial}{\partial x} = 0$).
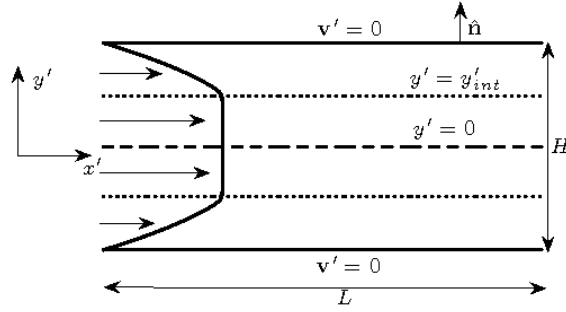

Figure 2: Steady pressure-driven flow in a two-dimensional (flow/flow-gradient plane) channel geometry in dimensional coordinates. At the walls, the no slip boundary condition, $\mathbf{v}' = 0$, is imposed. The profile shown is for a pressure forcing for which shear banding occurs showing the interface, y'_{int}, between the high shear rate flow adjacent to the walls and the lower shear rate flow in the center of the channel.

The dimensionless system of equations governing this 1D pressure-driven flow for the VCM model are:

$$0 = \mathcal{P} + \beta u_{,yy} + A_{xy,y} + 2B_{xy,y} \tag{15}$$

$$\mu\frac{\partial n_A}{\partial t} = \delta_A(2n_{A,yy} - A_{yy,yy}) + \frac{1}{2}c_{Beq}n_B^2 - c_{Aeq}n_A - \Xi \tag{16}$$

$$\mu\frac{\partial n_B}{\partial t} = 2\delta_B(n_{B,yy} - B_{yy,yy}) - c_{Beq}n_B^2 + 2c_{Aeq}n_A + 2\Xi \tag{17}$$

$$\mu A_{yy,t} + A_{yy} - n_A = \delta_A A_{yy,yy} + c_{Beq}n_B B_{yy} - c_{Aeq}A_{yy} - \Xi\frac{A_{yy}}{n_A} \tag{18}$$

$$\mu(A_{xy,t} - u_{,y}A_{yy}) + A_{xy} = \delta_A A_{xy,yy} + c_{Beq}n_B B_{xy} - c_{Aeq}A_{xy} - \Xi\frac{A_{xy}}{n_A} \tag{19}$$

10

$$\mu(A_{xx,t}-2u_{,y}\,A_{xy})+A_{xx}-n_A = \delta_A A_{xx,yy}+c_{Beq}n_B B_{xx}-c_{Aeq}A_{xx}-\Xi\frac{A_{xx}}{n_A} \quad (20)$$

$$\epsilon\mu B_{yy,t} + B_{yy} - \frac{n_B}{2} = 2\epsilon\left(\frac{\delta_B}{2}B_{yy,yy} - c_{Beq}n_B B_{yy} + c_{Aeq}A_{yy} + \Xi\frac{A_{yy}}{n_A}\right) \quad (21)$$

$$\epsilon\mu(B_{xy,t} - u_{,y}\,B_{yy}) + B_{xy} = 2\epsilon\left(\frac{\delta_B}{2}B_{xy,yy} - c_{Beq}n_B B_{xy} + c_{Aeq}A_{xy} + \Xi\frac{A_{xy}}{n_A}\right)$$
$$(22)$$

$$\epsilon\mu(B_{xx,t}-2u_{,y}\,B_{xy})+B_{xx}-\frac{n_B}{2} = 2\epsilon\left(\frac{\delta_B}{2}B_{xx,yy} - c_{Beq}n_B B_{xx} + c_{Aeq}A_{xx} + \Xi\frac{A_{xx}}{n_A}\right)$$
$$(23)$$

where $\Xi = \frac{2\xi\mu}{3}u_{,y}\,A_{xy}$.

3.2. Numerical Method

In the stability analysis to be discussed below we make no assumptions about the symmetry of the perturbed system of equations. Unlike [35, 34] in which the authors only consider symmetric (even) eigenmodes, we allow the system to select between even and odd modes. In order to accomplish this the equations must be solved across the entire channel ($-1/2 \leq y \leq 1/2$). The numerical complications that arise in solving the base state for the VCM model are discussed in [21] and in the case of the full channel, due to the symmetry of the zeroth order problem, there are two apparent slip boundary layers (one at each wall) and, during shear banding, two time-evolving interior layers (interface between the bands), symmetric about the centerline. The ADDS (adaptive domain decomposition spectral) method described in [21] to solve the half channel problem is easily adapted to the full channel by using a domain decomposition with five subdomains; this is done essentially by using the domain decomposition described in [21] reflected about the center (symmetry) line.

3.3. Results

In [21], the VCM model was investigated in 1D pressure-driven flow through a rectilinear microchannel. In that work it was shown that stress-orientation coupling has a nonlocal effect on the velocity profile in the chan-

11

nel. Specifically, with the use of no flux boundary conditions on the number density and stress, a boundary layer in the velocity and shear stress exists at the solid walls. The boundary layer in the velocity corresponds to an apparent slip layer and, for pressure driving forces smaller than the critical pressure-drop at which the onset of shear banding occurs ($\mathcal{P}_{crit}$), the dimensionless slip velocity is explicitly computed to be $u_s \simeq \frac{\mathcal{P}\delta}{2}$. In Fig.3(a) the steady-state velocity profiles for a dimensionless pressure gradient $\mathcal{P} = 1 < \mathcal{P}_{crit}$ are shown for $\delta = 0$ as well as for several nonzero values of the diffusivity parameter. The effects of diffusion and the resulting apparent slip layer at the wall are clearly visible for $\delta = 10^{-1}$. The increase in the velocity profile across the channel due to the apparent slip layer adds to the volumetric flow rate expected in the no slip ($\delta = 0$) case such that $\mathcal{Q} = \mathcal{Q}_{\delta=0} + \frac{\mathcal{P}\delta}{2} + O(\delta^2)$. For small diffusion lengths, $\ell_d << H$ (that is $\delta << 1$), the interfacial and boundary layers are very thin and remain well-separated from each other. This suggests that the specific boundary conditions applied at the wall have no effect on the interfacial instability as concluded in [51].

Above the critical pressure gradient, $\mathcal{P}_{crit}$, shear banding occurs and the flow develops a high shear rate region adjacent to each wall connected through a sharp interfacial layer to a low shear rate flow in the center of the channel. Fig.3(b) shows several shear banded velocity profiles for increasing values of $\mathcal{P} \geq \mathcal{P}_{crit}$ with $\delta = 10^{-3}$.

In Fig.4 the dimensionless volumetric flow rate, $\mathcal{Q} = \int_{-1/2}^{1/2} u(y)dy$, for startup of pressure-driven flow is plotted as a function of the dimensionless pressure gradient, $\mathcal{P}$, for $\delta = 10^{-2}$. For $\mathcal{P} < \mathcal{P}_{crit}^+$ and $\mathcal{P} >> \mathcal{P}_{crit}^+$, the VCM model is dominated by a single species (the 'A' species for small $\mathcal{P}$ and the short 'B' species for large $\mathcal{P}$). The resulting dimensionless volumetric flow rate can be found explicitly to be $\mathcal{Q} \simeq \frac{1}{12}\mathcal{P}$ and $\mathcal{Q} \simeq \frac{1}{12\mu\epsilon n_T}\mathcal{P}$ for small and large pressure-drops respectively [21]. At the onset of shear banding, corresponding to a value of the pressure gradient $\mathcal{P}_{crit}^+ \simeq 2.455$, there is a sudden jump in the volumetric flow rate. This phenomenon is commonly referred to as spurt and has been documented experimentally in pressure-driven channel and pipe flows of micellar solutions [29, 52, 53]. In Fig.4 we also show the volumetric flow rates computed by progressively decreasing the dimensionless pressure gradient from $\mathcal{P} = 10$ down to 0. A sudden drop in volumetric flow rate occurs during this ramp down at a critical value of the pressure gradient, $\mathcal{P}_{crit}^- \simeq 1.3485 < \mathcal{P}_{crit}^+$, the critical pressure gradient in startup. The non-uniqueness of the critical pressure gradient is indicative
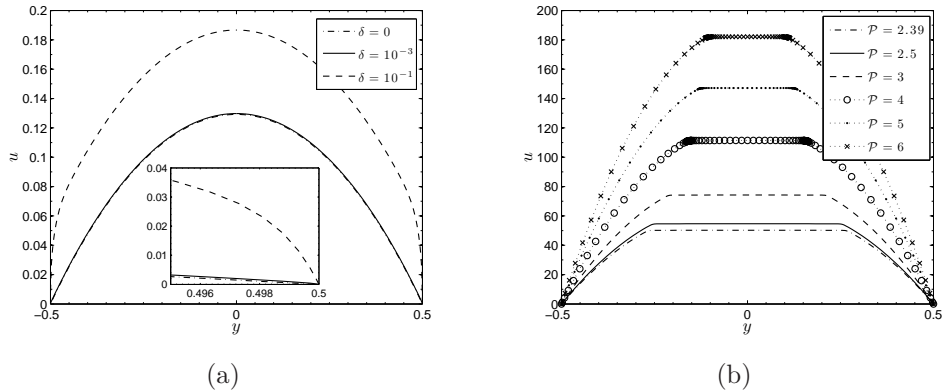
(a)   (b)

Figure 3: (a) Velocity profiles for the VCM model in the linear viscoelastic region ($\mathcal{P} = 1 < \mathcal{P}_{crit}$). For $\delta = 0$ the expected parabolic profile develops. The addition of diffusive effects in both the stress and number density coupled with no flux boundary conditions creates an apparent slip layer at the wall and increases the flow rate through the channel. This layer corresponds to an apparent slip velocity, $u_s \simeq \frac{\mathcal{P}\delta}{2}$ [21] and this increase in the velocity adds to the volumetric flow rate such that, for $\mathcal{P} = 1$, $\mathcal{Q} = \mathcal{Q}_{\delta=0} + \delta/2$. (b) Shear banded velocity profiles of the VCM model for various values of the imposed pressure gradient, $\mathcal{P} \geq \mathcal{P}_{crit}$, for $\delta = 10^{-3}$.

of hysteresis in the pressure-driven flow of the VCM model. We note here that all results on stability of the VCM model presented in this work are for steady base states obtained from start-up of pressure-driven flow.

4. Linear Stability Analysis

4.1. Flow/Flow gradient plane

We consider the linear stability of the base state determined above due to perturbations in the flow/flow gradient plane ($x - y$ plane). In this formulation the velocity field takes the form $\mathbf{q} = (u^0(y) + u^1(y)S, v^1(y)S, 0)$, where $u^0(y)$ denotes the base state found above, and $S = se^{i(kx-\omega t)}$ where k is the wavenumber in the flow direction, and $\omega = \omega_R + i\omega_I$ is the growth rate (eigenvalue) such that $\omega_I > 0$ denotes growth of disturbances (instability). Here s indicates the (infinitesimal) amplitude of the perturbations. Similarly the number density and stress of each species are expanded as $() = ()^0 + ()^1 S$. Conservation of mass for this system states that $iku^1 + v^1(y) = 0$. To guarantee this we introduce a streamfunction ψ where $u^1 = \psi_{,y}, v^1 = -ik\psi$.
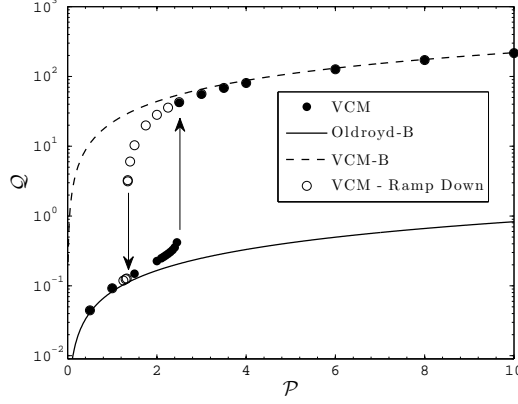
13

Figure 4: A comparison of the dimensionless volumetric flow rate down the channel for the VCM (startup, •; ramp down, ∘) and Oldroyd-B models as the imposed pressure gradient increases. For the Oldroyd-B model, the flow rate increases linearly with the pressure gradient ($\mathcal{Q} = \frac{1}{12(1+\beta)}\mathcal{P}$). The dashed line corresponds to the volumetric flow rate pressure drop relationship obtained for flow of the VCM model dominated by the 'B' species and solvent only ($Q = \frac{1}{12(\mu\epsilon n_T+\beta)}\mathcal{P}$). Note that the axes are semilogarithmic to accommodate the sudden spurt in the VCM model at $\mathcal{P}_{crit}^{+} \simeq 2.455$. The sudden drop in volumetric flow rate during the ramp down occurs at $\mathcal{P}_{crit}^{-} \simeq 1.3485$. The non-uniqueness of the critical pressure gradient is indicative of hysteresis in the pressure-driven flow of the VCM model. Here $\beta = 7 \times 10^{-5}$, $\mu = 1.9$, $\epsilon = 6.27 \times 10^{-4}$, $n_T = 3.134$ and $\delta = 10^{-2}$.

Substitution into the full equations and retaining only those terms first order in s, the resulting linear system to be solved for the eigenvalues $\omega(k; y)$ is:

Momentum:

$$ik(p^1 + n_A^1 + n_B^1 - A_{xx}^1 - 2B_{xx}^1 - 2\beta ik\psi_{,y}) - A_{xy,y}^1 - 2B_{xy,y}^1 - \beta(\psi_{,yyy} + k^2\psi_{,y}) = 0 \quad (24)$$

$$ik(-A_{xy}^1 - 2B_{xy^1} - \beta(\psi_{,yy} + k^2\psi)) + p_{,y}^1 + n_{A,y}^1 + n_{B,y}^1 - A_{yy,y}^1 - 2B_{yy,y}^1 + 2\beta ik\psi_{,yy} = 0 \quad (25)$$

14

Number Density:

$$(iku^0 - i\omega)\mu n_A^1 - ik\mu\psi n_{A,y}^0 - \delta_A(-2k^2n_A^1 + 2n_{A,yy}^1) + \delta_A(2ikA_{xy,y}^1 - k^2A_{xx}^1 + A_{yy,yy}^1)$$
$$= c_{Beq}n_B^1n_B^0 - c_A^1n_A^0 - c_A^0n_A^1 \tag{26}$$

$$(iku^0 - i\omega)\mu n_B^1 - ik\mu\psi n_{B,y}^0 - 2\delta_B(-k^2n_B^1 + n_{B,yy}^1) + 2\delta_B(2ikB_{xy,y}^1 - k^2B_{xx}^1 + B_{yy,yy}^1)$$
$$= -2(c_{Beq}n_B^1n_B^0 - c_A^1n_A^0 - c_A^0n_A^1) \tag{27}$$

Stress:

$$-i\omega\mu\mathbf{A}^1 - i\mu k\psi\mathbf{A^0}_{,y} + ik\mu u^0\mathbf{A}^1 - n_A\mathbf{I} - \mu\mathbf{D}_A - \delta_A(\mathbf{A}_{,yy}^1 - k^2\mathbf{A}^1)$$
$$= c_{Beq}(n_B^0\mathbf{B}^1 + n_B^1\mathbf{B}^0) - c_A^0\mathbf{A}^1 - c_A^1\mathbf{A}^0 \tag{28}$$

$$\epsilon(-i\omega\mu\mathbf{B}^1 - i\mu k\psi\mathbf{B^0}_{,y} + ik\mu u^0\mathbf{B}^1) - \frac{n_B^1}{2}\mathbf{I} - \epsilon\mu\mathbf{D}_B - \delta_B(\mathbf{B}_{,yy}^1 - k^2\mathbf{B}^1)$$
$$= -2\epsilon(c_{Beq}(n_B^0\mathbf{B}^1 + n_B^1\mathbf{B}^0) - c_A^0\mathbf{A}^1 - c_A^1\mathbf{A}^0) \tag{29}$$

where

$$c_A^1 = \frac{\mu\xi}{3}\left[\frac{2u_{,y}^0A_{xy}^1 + \dot{\boldsymbol{\gamma}}^1 : \mathbf{A}^0}{n_A^0} - \frac{\dot{\boldsymbol{\gamma}}^0 : \mathbf{A}^0 n_A^1}{(n_A^0)^2}\right], \tag{30}$$

$$\dot{\gamma}_{21}^0 = \dot{\gamma}_{12}^0 = u_{,y}^0, \dot{\gamma}_{ii}^0 = 0 \tag{31}$$

and

$$\dot{\gamma}_{21}^1 = \dot{\gamma}_{12}^1 = k^2\psi + \psi_{,yy} \tag{32}$$

$$\dot{\gamma}_{11}^1 = 2ik\psi_{,y} \tag{33}$$

$$\dot{\gamma}_{22}^1 = -2ik\psi_{,y} \tag{34}$$

$$D_{A11} = 2(A_{xx}^0ik\psi_{,y} + A_{xy}^0\psi_{yy} + A_{xy}^1u_{,y}^0) \tag{35}$$

$$D_{A21} = D_{A12} = k^2\psi A_{xx}^0 + u_{,y}^0A_{yy}^1 + \psi_{,yy}A_{yy}^0 \tag{36}$$

$$D_{A22} = 2(A_{yx}^0k^2\psi - A_{yy}^0ik\psi_{,y}) \tag{37}$$

The terms of the tensor $\mathbf{D}_B$ coupling the base flow and the perturbation are identical to those of $\mathbf{D}_A$ with all A's replaced by B's.

This system constitutes 10 linear differential equations for the 10 unknowns $(\psi, p^1, n_A^1, n_B^1, A_{xx}^1, A_{xy}^1, A_{yy}^1, B_{xx}^1, B_{xy}^1, B_{yy}^1)$ as a function of k and ω,

so that for each k we can determine the eigenvalues ω. We are interested in the eigenvalue with the largest imaginary part, $\omega^* = \max(\omega_I)$, which represents the most unstable mode.

The boundary conditions of no flux for the first order perturbation to the conformation and number density of each species at the boundaries, and zero perturbed velocity at the walls ($y = \pm 1/2$), are given by:

$$\frac{2\partial n_A^1}{\partial y} - ikA_{xy}^1 = 0 \tag{38}$$

$$\frac{2\partial n_B^1}{\partial y} - 2ikB_{xy}^1 = 0 \tag{39}$$

$$\frac{\partial A_{ij}^1}{\partial y} = 0 \tag{40}$$

$$\frac{\partial B_{ij}^1}{\partial y} = 0 \tag{41}$$

$$u^1 = v^1 = 0. \tag{42}$$

4.2. Numerical Method

The system of equations (24)-(29) constitute a generalized matrix eigenvalue problem of the form

$$[\mathbf{A} - \omega\mathbf{B}]\,\mathbf{x} = 0 \tag{43}$$

where the (mass) matrix $\mathbf{B}$ is singular resulting from the lack of a time derivative in the inertialess momentum equations and boundary conditions. Due to the singular nature of $\mathbf{B}$ there exist eigenvalues of (43) which are infinite. These infinite eigenvalues affect the solution of the system by appearing as large numerical values which one may not be able to distinguish from spurious modes. To avoid the corruption in the structure of the eigenvalue spectrum, we use the method described by [54] to map the infinite eigenvalues to one or more points in the complex plane leaving the true, finite eigenvalues of the system unperturbed.

We first simplify the equations and introduce boundary conditions for the eigenvectors. Equations (24) and (25) can be combined to eliminate the pressure, p, leaving a fourth order differential equation for the stream function ψ. The boundary conditions of no-flux for the stresses and number densities

16

are given in equations (38)-(41). Given the no-slip boundary condition for the velocities (42), the resulting boundary conditions for the stream function are $\psi = 0$ and $\psi,_y = 0$ at the walls.

As was mentioned in Section 3.2, the 1D base state solution is obtained through the ADDS method [21] in order to track the time-dependent evolution in the sharp nonlinear interface and ensure that the steady state is fully resolved. The ADDS method incorporates the domain decomposition patching method [55] which requires conditions at the intersection of the sub-domains for which we use the interface continuity conditions [55] (that is the function and its derivative are equal at the intersection). The use of these interface conditions, however, produces a repeated condition on the stream-function at the interface which creates an underdetermined system of equations. To resolve this matter the steady base state solution is mapped onto a single Chebyshev domain through barycentric Lagrange interpolation [56] for use subsequently in the solution of the eigenvalue problem. This method has been tested against using a single Chebyshev domain to discretize the steady base state and subsequently in the solution of the eigenvalue problem, and the results agree to within 0.1%.

To determine the robustness of this scheme, we first test our method against previous published results for linear stability in planar Poiseuille flow. First, we solve the eigenvalue problem for the Oldroyd-B model (corresponding to the VCM model with $\delta = 0, \epsilon = 0, \mu = 1, \xi = 0, c_{Aeq} = c_{Beq} = 0$) with $\beta = 0.2$ to be compared with results from [36, 38]. Fig.5(a) shows the computed eigenspectrum for the Oldroyd-B model in the channel flow. For this model there are exactly two continuous branches to the eigenspectrum, one corresponding to the upper convected Maxwell model located at $\text{Im}(\omega) = -1$ (Fig.5(c)) and a second that arises from the introduction of a solvent viscosity located, for our chosen scaling of the stress, at $\text{Im}(\omega) = -(1 + \beta)/\beta$ (Fig.5(b)). In addition, there are several discrete eigenmodes (these are discussed in detail in [38]) corresponding to both the upper convected Maxwell and solvent portions of the problem.

The role of stress diffusion in the Oldroyd-B model has also been considered [37] and the authors showed that, in the absence of inertia, the model is still stable, however, both branches of the continuous spectra shown in Fig.5 become highly distorted. As can be seen in the eigenspectrum of this model shown in Fig.6 there are still remnants of the two distinct continuous spectra seen in Fig.5 however, the overall structure has been destroyed along with the addition of many discrete modes along the line $\text{Im}(\omega) = -1$.
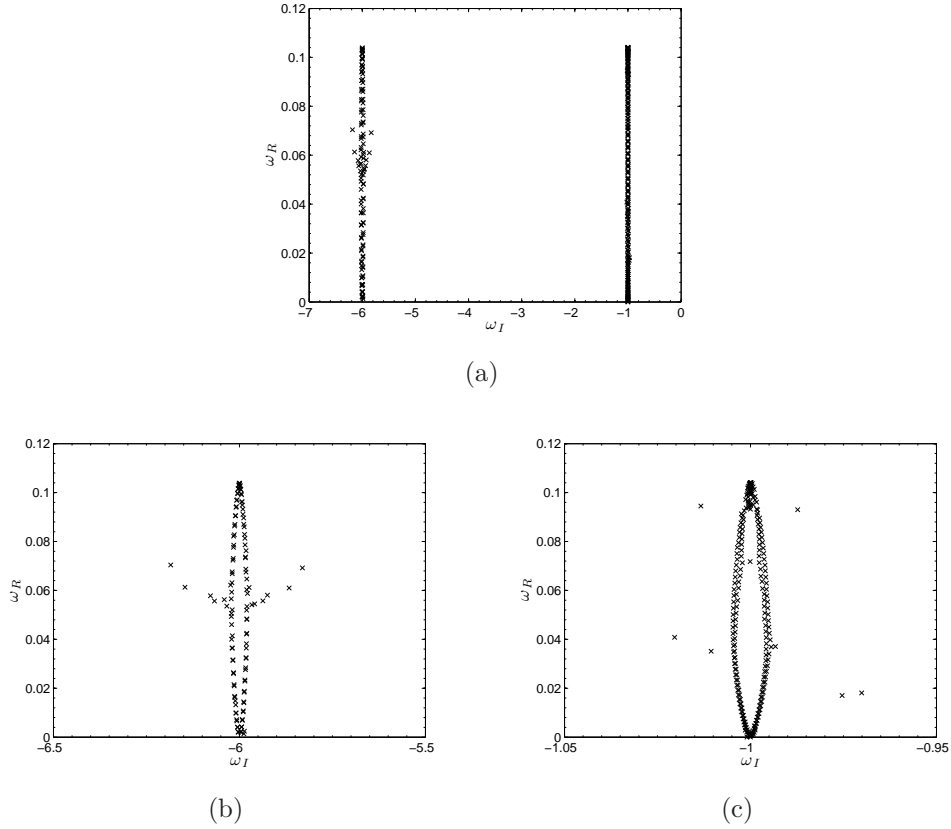
17

Figure 5: (a) Eigenspectrum of the Oldroyd-B model ($\delta = 0, \epsilon = 0, \mu = 1, \xi = 0, c_{Aeq} = c_{Beq} = 0$) for $\mathcal{P} = 1$, $\beta = 0.2$, $k = 1$ using $N = 128$ Chebyshev nodes. (b) Local enlargement of the contribution to the eigenspectrum corresponding to the addition of the solvent viscosity in the Oldroyd-B model. (c) Local enlargement of the eigenspectrum branch corresponding to the upper convected Maxwell portion of the Oldroyd-B model.

We also tested the method against results reported in [42] for the Johnson-Segalman (JS) model. In this work the authors used a full nonlinear calculation to obtain the most unstable eigenmodes and these were reported in the dispersion relations. The most unstable mode found by solving the eigenvalue problem for the JS model through our method compare well with the results from [42]. In addition to obtaining the most unstable mode we are able to capture the full eigenspectrum of the JS model to ensure that the most unstable discrete modes are sufficiently resolved and this is shown in
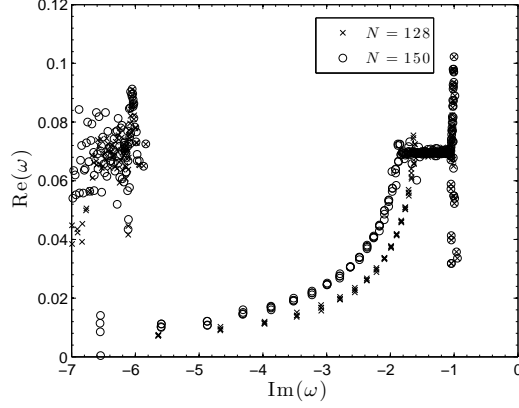
18

Figure 6: Eigenspectrum of the Oldroyd-B model ($\epsilon = 0, \mu = 1, \xi = 0, c_{Aeq} = c_{Beq} = 0$) for $\mathcal{P} = 1$, $\beta = 0.2$, $k = 1$ with the addition of stress diffusion ($\delta = 10^{-5}$) using $N = 128$ and $N = 150$ Chebyshev nodes to distinguish the discrete eigenmodes.
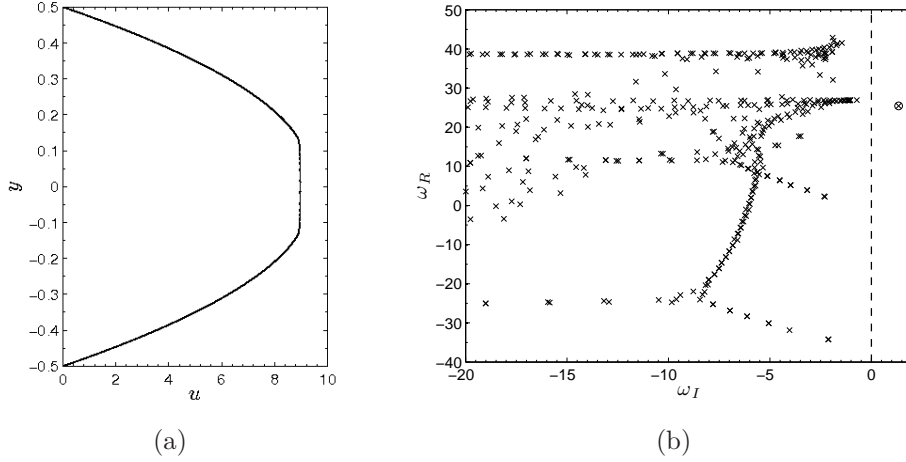

(a)

(b)

Figure 7: (a) Shear-banded velocity profile of the Johnson-Segalman model for $\mathcal{P} = 4$, $\beta = 0.05$ and $\delta = \ell_d^2/H^2 = 10^{-4}$ along with the model parameters given in [42]. (b) Previously unseen eigenspectrum of the Johnson-Segalman model for the corresponding shear-banded base state in (a) for a wavenumber, $k = 3$, such that the base state is unstable with the most unstable eigenvalue (circled) at $\omega^* = \max(\omega_I) = 1.345$. Here we use $N = 250$ Chebyshev nodes.

19

Fig.7 below.

4.3. Results

Below the shear banding threshold, for small pressure driving forces, $\mathcal{P} < \mathcal{P}_{crit}$, the VCM model is well approximated by the quasilinear Oldroyd-B model which has been shown to be linearly stable in inertialess planar Poiseuille flow both without diffusion [36, 38] and with diffusion [37], thus our primary concern is with the linear stability of the shear-banded base states.

Using the Johnson-Segalman model with diffusion, [42] showed that shear banded profiles in this pressure-driven channel flow can be linearly unstable. Using a fully nonlinear code, they tracked the early-time growth and determined the dispersion relation $\omega(k)$. Using various sizes of the diffusive interfacial thickness that characterizes the width of the shear band interface ($\ell_d = \sqrt{D\lambda}$ so that $\delta \equiv \ell_d^2/H^2$), [42] showed that there exists a linear reduction in growth rate and ℓ_d. As the width of the interface of the shear band is increased, the growth rates decreased and the flow becomes increasingly stable. In the fully nonlinear code, the system selects solutions that exhibit either even (varicose or sausage-like) or odd (sinuous or snake-like) symmetry and it was found that the most unstable eigenmode corresponds to the sinuous mode. The wavelength of the mode corresponding to the peak of the dispersion relationship was determined as a function of the imposed pressure gradient. For pressure gradients deep within the shear-banding regime this wavelength was found to be $l_w/H = 2\pi/k \sim O(2)$, or twice the gap width, which is consistent with the presence of secondary velocity rolls [57, 58]. However, these authors also point out that the JS model is highly oversimplified and that the values used for the interface parameter ℓ_d were too small to be considered appropriate for microchannel flows of micellar fluids. To this end we will investigate the stability of shear-banded base states of the VCM model with a range of values for $\delta = \ell_d^2/H^2$ that are appropriate for both microchannels and macrochannels.

Like the Johnson-Segalman model, following the onset of shear banding, the velocity profile predicted by the VCM model can become unstable to streamwise perturbations. Fig.8 shows the dispersion relation constructed by plotting the growth rate of the most unstable mode versus wavenumber for various pressure gradients $\mathcal{P}$ with a small diffusivity parameter, $\delta = 10^{-3}$, close to the minimum expected for microchannels. At the onset of shear banding (approximately $\mathcal{P} = 2.39$ for this value of δ) the flow spurts and the

growth rate of one discrete eigenmode becomes positive. As $\mathcal{P}$ increases further the width of the unstable region and the range of unstable wavenumbers decreases. Initially the value of the maximum growth rate remains relatively constant and then decreases as $\mathcal{P}$ is increased further. Unlike [42], we find that the wavelength ($l_w/H = 2\pi/k$) of the most unstable disturbance (corresponding to the peak of the dispersion relation) is $l_w/H \sim O(3)$, or three times the gap width. Fielding also determined for the JS model that the wavelength of instability at the onset of shear banding is very small, consistent with a very thin high shear rate band. In contrast to [42], we find that the dimensionless wavelength approaches a finite value, $l_w/H = 3$ in the limit $\mathcal{P} \to \mathcal{P}_{crit} \simeq \mathcal{P}_{crit}^+$.

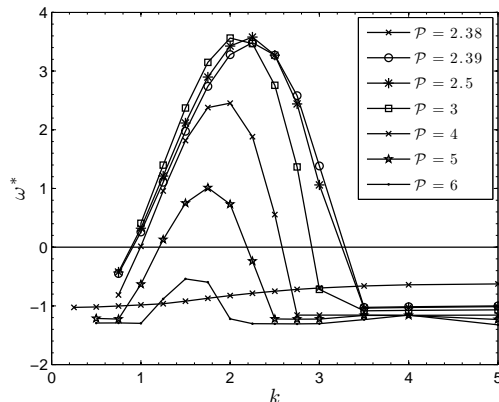
Figure 8: Dispersion relation for the VCM model ($\beta = 7 \times 10^{-5}$, $\mu = 1.9$, $c_{Aeq} = 0.9$, $c_{Beq} = 1.4$, $\epsilon = 6.27 \times 10^{-4}$, $\xi = 0.3$) showing the growth rate of the most unstable mode versus wavenumber for a fixed diffusivity $\delta = 10^{-3}$ for various pressure gradients within the shear banding regime (see Fig.3(b) for corresponding velocity profiles). $\mathcal{P}_{crit} = 2.39$ corresponds approximately to the onset of shear banding for this value of the diffusivity parameter.

As was shown in both [37] and [42], diffusion plays a stabilizing role and thus one would expect that there is a critical diffusivity parameter δ at which the flow is restabilized. This effect can be seen in Fig.9(b). Here we plot the dispersion relation for a fixed pressure gradient in the shear banding regime ($\mathcal{P} = 2.5$) for values of the dimensionless diffusivity $\delta = \ell_d^2/H^2$. Restabilization of the base flow occurs between $\delta = 4.25 \times 10^{-3}$ and $\delta = 4.5 \times 10^{-3}$, and unlike the sudden transition from stability to instability seen in Fig.8

as the flow spurts, the restabilization as δ changes is much smoother. Extensive calculations show that the most unstable mode, $\omega^* = \max(\omega_I)$, for the VCM model decrease linearly with increasing diffusivity. We have also computed the next order correction to the fit and find that $\omega^* = \omega_0^* - b\delta + a\delta^2$ $(a, b > 0)$, thus the growth rate decreases more slowly with increasing diffusivity than the linear relationship predicted by [42]. The changes in the base velocity profile Fig.9(a) as δ is incremented from 10^{-3} to 10^{-2} are imperceptible, except very close to the kink at the shear band (see insert). Clearly the unstable mode is an interfacial mode arising from the large change in the effective viscosity and normal stress difference across the interface.
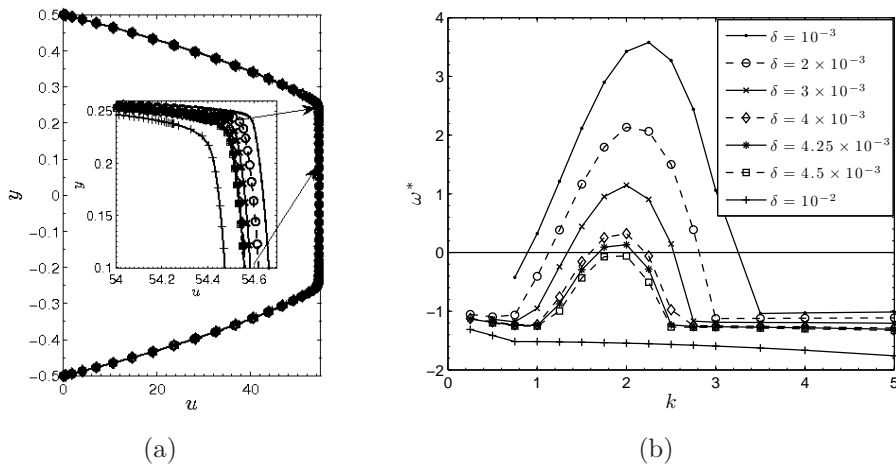

(a)   (b)

Figure 9: (a) Velocity profile of the VCM model for $\mathcal{P} = 2.5$ for various values of the diffusivity parameter, δ. The inset shows an enlargement of the interfacial region between the high and low shear rate bands showing the dependence of y_{int} on δ and the sharpness of the transition region. (b) Dispersion relation showing the variation in the growth rate and wavenumber of the most unstable mode for a fixed pressure drop $\mathcal{P} = 2.5$ in the shear banding regime showing the stabilizing effect of increasing diffusion. The same symbols and line styles are used in both figures.

To ensure that these interfacial modes of instability are sufficiently resolved, the eigenspectra are plotted for various numbers of Chebyshev nodes. In Fig.10 we plot the full eigenspectrum for $\mathcal{P} = 2.5$, $\delta = 10^{-3}$ and $k = 2$ and show subsequent enlargements so that the structure of the entire spectrum can be resolved. There is exactly one unstable mode (seen in Fig.10(d)) which we have resolved to two decimal places with the number of discretiza-

tion nodes employed to be $\omega = 85.58 + 3.42i$. This mode is mesh converged and hence it is a discrete eigenmode that is well separated from the remainder of the spectrum. Thus there is no possibility of the mode disappearing into a continuous branch of the spectrum as was seen in [38] for the UCM model.
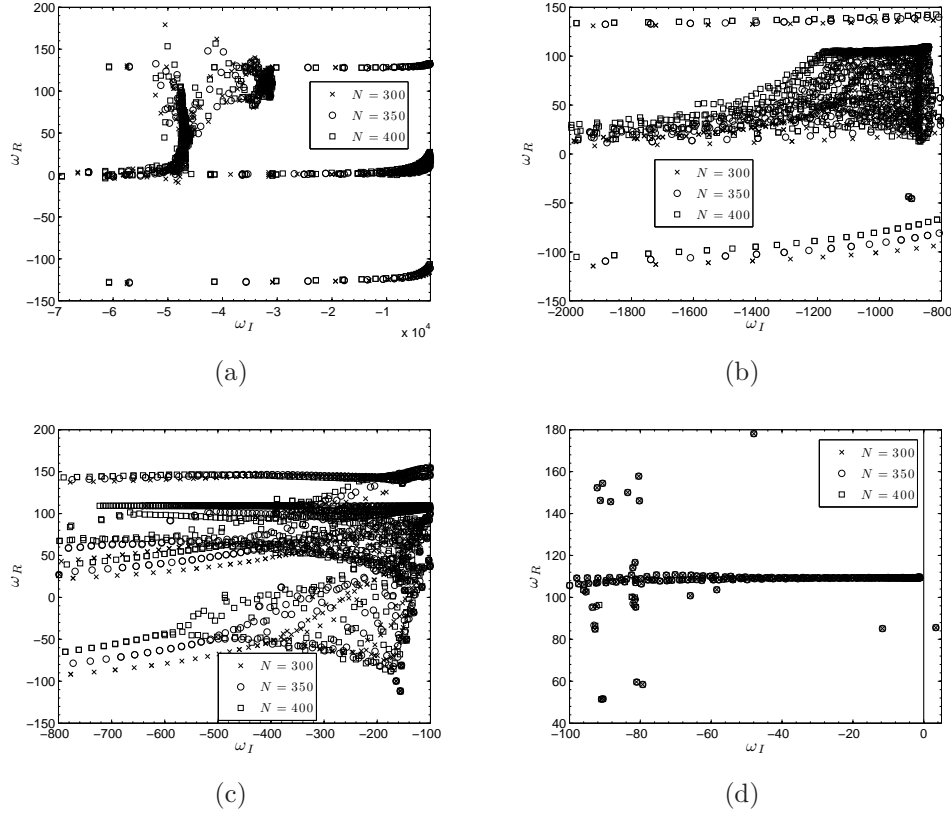

Figure 10: Enlarged views of the full eigenspectrum of the VCM model for $\mathcal{P} = 2.5$, $\delta = 10^{-3}$ and $k = 2$: (a) $-7 \times 10^4 \le \omega_I \le -2000$, (b) $-2000 \le \omega_I \le -800$, (c) $-800 \le \omega_I \le -100$ and (d) $-100 \le \omega_I \le \omega^*$ for three different degrees of Chebyshev discretization ($N = 300, 350, 400$). In the final image (d) the unstable mode is clearly separated from the rest of the stable spectrum and is mesh converged (to 2 decimal places) with $\omega = 85.58 + 3.42i$.

In Fig.11 and Fig.12 we plot the eigenfunctions for this unstable mode ($\mathcal{P} = 2.5$, $\delta = 10^{-3}$ and $k = 2$) corresponding to the perturbed velocity (u^1) (and streamfunction ψ) and micellar shear stress ($A_{xy}^1 + 2B_{xy}^1$) respectively.

23

We note that these eigenfunctions break the symmetry of the base state. These modes are odd (sinuous) as was observed in [42] for the Johnson-Segalman model. The steep spatial gradients in the eigenfunctions precisely at the location of the interface connecting the shear bands suggests that the interface will become locally distorted and wavy in a similar manner to the full nonlinear calculations presented by Fielding for the JS model [42]. The perturbation to the stress $A_{xy}^1 + 2B_{xy}^1$ is symmetric about the midplane, $y = 0$, and when added to the antisymmetric base state shown in Fig.12(a) will break the symmetry of the resulting flow state.

In Fig.9(b) it was shown that the flow is only unstable when the kink in the velocity profile at the shear band interface is sufficiently sharp, corresponding to a critical value of the dimensionless diffusivity $\delta < \delta_{crit}$. As $\delta = D_A \lambda_A / H^2$ increases (for example by shrinking the channel dimension), the maximum growth rate decreases and the range of wavenumbers for which instability occurs also decreases. This stabilizing effect of the diffusive coupling between the microstructure and the velocity field can also be seen for other pressure driving forces within the shear banding regime. A neutral stability curve for which $\omega_I(k; \mathcal{P}, \delta) = 0$ for several values of δ is plotted in Fig.13(a) determining the range of linear instability as a function of both $\mathcal{P}$ and k. As δ increases, both the maximum pressure gradient and range of wavenumbers for which the base flow is unstable progressively decrease, collapsing eventually to a single value. This can be further seen in Fig.13(b) where the neutral stability curve in $\delta - \mathcal{P}$ space is shown. As δ increases, the minimum value of the critical pressure gradient for onset of spurt (and instability) increases slowly and the maximum pressure gradient decreases steadily until the curves intersect and the flow becomes globally stable beyond a critical dimensionless diffusivity $\delta_{crit} \simeq 4.51 \times 10^{-3}$. Beyond this point the base flow still exhibits a spurt transition (see Fig.10 in [21]) but the thickness of the shear band becomes sufficiently wide and viscous stresses from the solvent and the shorter 'B' species become sufficiently large to dampen out the perturbations induced by the local variations in the viscoelastic stresses of the 'A' species that exist at the interfacial shear band. Due to the hysteretic nature of the pressure-driven flow of the VCM model the critical value of the dimensionless pressure gradient, $\mathcal{P}_{crit}$ is not unique with $\mathcal{P}_{crit}^- < \mathcal{P}_{crit}^+$. Exploratory calculations, not presented, show that for $\mathcal{P} \geq \mathcal{P}_{crit}^-$ the base state solutions obtained from ramp down calculations exhibit a window of linear instability. Thus, we expect the lower branch of the neutral stability curve in Fig.13(b) to move down increasing the window of instability.
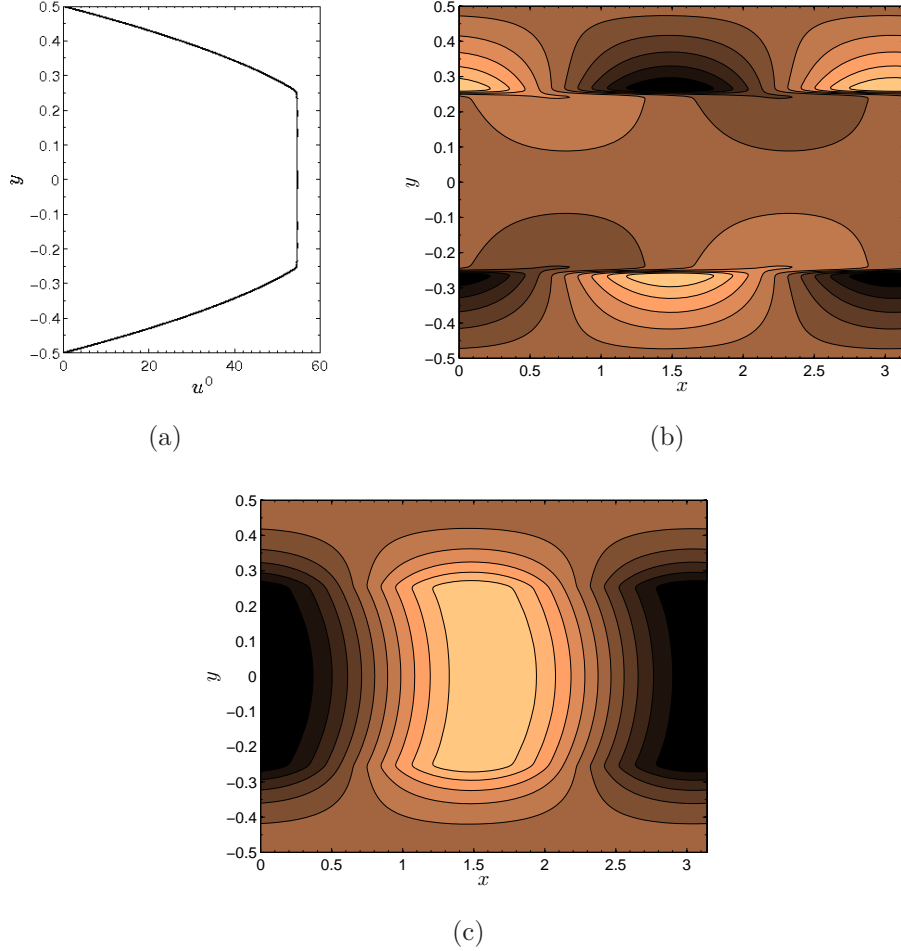
(a)

(b)

(c)

Figure 11: (a) Base state banded velocity profile of the VCM model for $\mathcal{P} = 2.5$ and $\delta = 10^{-3}$. (b) Eigenfunction of the most unstable mode for $k = 2$ corresponding to the perturbed velocity $u^1 = \frac{\partial \psi}{\partial y}$ that is superposed on the base state velocity u^0 in (a). The eigenfunction breaks the symmetry of the base state and thus produces a sinuous (snake-like) flow. The sharp localized variation in the perturbed velocity at the interface between shear bands suggests that the interface becomes locally distorted in this unstable flow and that the largest variations in the velocty profile are in the shear band and not in the low shear rate core. (c) Corresponding streamfunction, ψ, of the perturbed flow. The cusps in the profile are located at interface and indicate steep spatial gradients of ψ resulting in the interfacial disturbance in the perturbed velocity seen in (b).
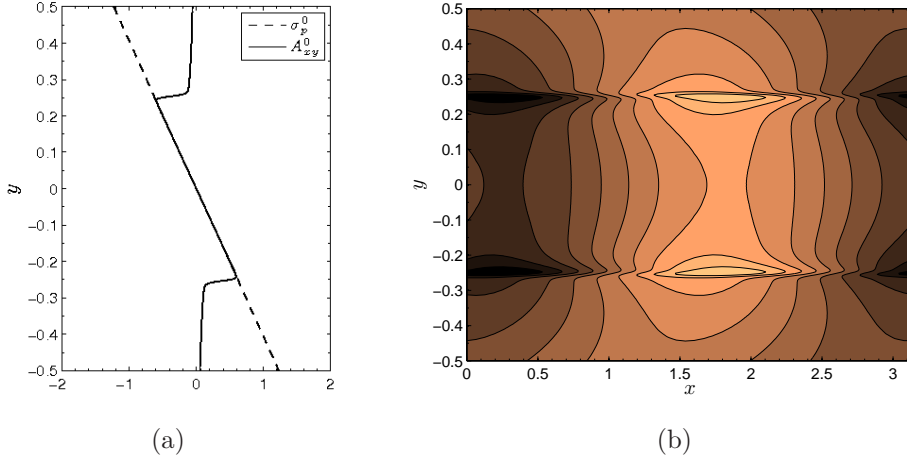
25

$$\text{(a)} \qquad\qquad\qquad\qquad\qquad \text{(b)}$$

Figure 12: (a) Base state profile of the contribution to the total shear stress of the long 'A' species, A_{xy}^0, and the (almost) linear variation in the total polymer shear stress, $\sigma_P^0 = A_{xy}^0 + 2B_{xy}^0$, across the channel of the VCM model for $\mathcal{P} = 2.5$ and $\delta = 10^{-3}$. (b) Eigenfunction of the most unstable mode for $k = 2$ corresponding to the perturbation to the micellar shear stress $A_{xy}^1 + 2B_{xy}^1$ that is added to the base state micellar shear stress $A_{xy}^0 + 2B_{xy}^0$. The perturbation $A_{xy}^1 + 2B_{xy}^1$ is symmetric about the midplane $y = 0$ and when added to the base state in (a) will break the symmetry of the resulting flow state.

5. Summary

We have investigated the linear stability of steady rectilinear pressure-driven flow of the VCM model. The VCM model has been developed to model the flow of entangled fluids such as wormlike micellar solutions that can exhibit shear-banding transitions above a critical stress. Before the onset of shear banding the model behaves like an Oldroyd-B model and plane Poiseuille flow is linearly stable in this regime in the absence of inertial effects. However, at the onset of shear banding, the flow exhibits a sudden spurt transition and the 1D base state of the VCM model can become unstable depending upon the values of the constitutive model parameters. Because of the sharp local variations in the base velocity profile, a Chebyshev pseudospectral approach with large number of collocation nodes ($N \geq 128$) is required to resolve both the base flow and the eigenspectrum of the perturbations. The characteristics of the instability observed for the VCM model are similar to those predicted in [42] for the Johnson-Segalman model. The mode of instability is an odd (sinuous) eigenmode, however,
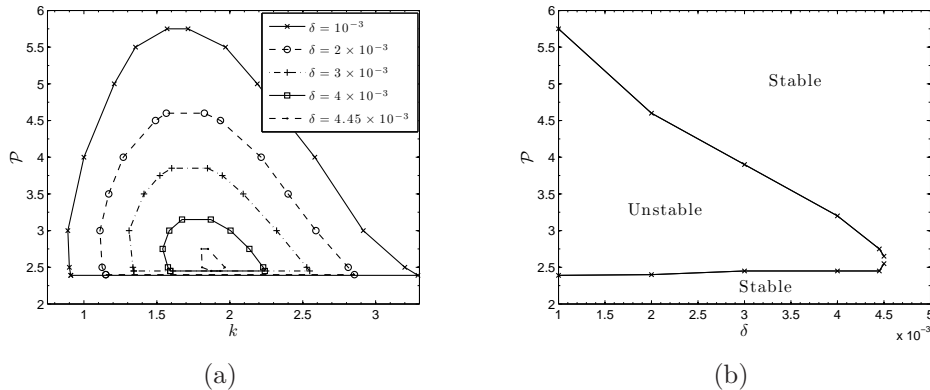
26

Figure 13: (a) Neutral stability curves of the VCM model for varying values of the diffusivity parameter, δ, in startup of pressure-driven flow showing the decreasing region of instability in the $k-\mathcal{P}$ plane as δ increases. (b) Neutral stability curve for the VCM model in the $\delta - \mathcal{P}$ plane in start-up of pressure-driven flow. The critical value of δ at which the flow is restabilized is approximately $\delta_{crit} = 4.51 \times 10^{-3}$ at which the curves intersect at approximately $\mathcal{P} = 2.6$. The bottom branch of this curve will be lower in ramp down due to the hysteretic nature of the pressure-driven flow of the VCM model where instead $\mathcal{P}_{crit}^- < \mathcal{P}_{crit}^+$.

the wavelengths of the most unstable mode, $l_{w,max}/H = 2\pi/k_{max}$, for the two models differ from $l_{w,max}/H \simeq 2$ for the JS model to $l_{w,max}/H \simeq 3$ for the VCM model (i.e. by about a gap width). In particular, sinuous streamwise instability is to be expected whenever the velocity variation across the shear band is sufficiently sharp, corresponding to a dimensionless diffusivity $\delta_{crit} = D_A \lambda_A/H^2 \leq 4.51 \times 10^{-3}$. As the length scale of the channel is reduced (e.g. in a microfluidic device), nonlocal effects become progressively more important and the flow becomes increasingly more stable. For the values of $D_A = 0.9 \times 10^{-8} \mathrm{m}^2/\mathrm{s}$, $\lambda_A = 0.0185\mathrm{s}$ reported in [14] for a CTAB micellar solution this corresponds to channels with length scales $H \lesssim 192\mu\mathrm{m}$. Sinuous modes of instability in the flow direction have recently been reported in experiments with wormlike micelles in pressure-driven pipe flows [29]. Sinuous variations in the interface position in the flow direction were also computed for planar channel flow [42]. However, very recent experimental observations of the 3D kinematics in micellar solutions following the onset of instability in both Taylor-Couette and plane Poiseuille flow show that perturbations are also observed in the 'neutral' or cross-channel (i.e. vorticity) direction

27

[30, 25]. The work of [28] on the Johnson-Segalman model suggests that instabilities in the vorticity direction are driven by a jump in the second normal stress difference, which is zero for the VCM model. The absence of a Squire's theorem for the VCM model means that it cannot be guaranteed that two-dimensional disturbances are the most unstable, and a logical extension to the present work is consideration of three-dimensional disturbances with $\mathbf{k} = \{k_x, k_z\}$. Ultimately full nonlinear simulation is necessary to assess the evolution in the amplitude of the perturbations and the structure of the saturated three-dimensional and/or time-dependent state.

Acknowledgments

References

[1] M.E. Cates. Reptation of living polymers: Dynamics of entangled polymers in the presence of reversible chain-scission reactions. Macromolecules, 20:2289–2296, 1987.

[2] Y.T. Hu and A. Lips. Kinetics and mechanism of shear banding in entangled micellar solutions. J. Rheol., 49:1101–1027, 2005.

[3] E. Miller and J.P. Rothstein. Transient evolution of shear banding in wormlike micelle solutions. J. Non-Newtonian Fluid Mech., 143:22–37, 2007.

[4] P. Boukany and S.Q. Wang. Use of particle-tracking velocimetry and flow birefringence to study nonlinear flow behavior of entangled wormlike micellar solution: From wall slip, bulk disentanglement to chain scission. Macromol., 41:1455–1464, 2008.

[5] P.T. Callaghan. Rheo NMR and shear banding. Rheol. Acta, 47:243–255, 2008.

[6] M.E. Cates. Flow behavior of entangled surfactant micelles. J. Phys. Condens. Matter, 8:9167–9176, 1996.

[7] P.D. Olmsted, O. Radulescu, and C.Y.D. Lu. Johnson-Segalman model with a diffusion term in cylindrical Couette flow. J. Rheol., 44:257–275, 2000.

[8] P.A. Vasquez, G.H. McKinley, and L.P. Cook. A network scission model for wormlike micellar solutions I: Model formulation and homogeneous flow predictions. J. Non-Newtonian Fluid Mech., 144:122–139, 2007.

[9] L. Zhou, P.A. Vasquez, L.P. Cook, and G.H. McKinley. Modeling the inhomogeneous response and formation of shear bands in steady and transient flows of entangled liquids. J. Rheol., 52:591–623, 2008.

[10] M.E. Cates and S.M. Fielding. Rheology of giant micelles. Advances in Physics, 55:799–879, 2006.

[11] S.M. Fielding. Complex dynamics of shear banded flows. Soft Matter, 2:1262–1279, 2007.

[12] P.D. Olmsted. Perspectives on shear banding in complex fluids. Rheol. Acta, 47:283–300, 2008.

[13] S. Lerouge and J.-F. Berret. Shear-induced transitions and instabilities in surfactant wormlike micelles. In Advances in Polymer Science. Springer-Verlag, 2009.

[14] M.E. Helgeson, P.A. Vasquez, N.J. Wagner, and E.W. Kaler. Rheology and spatially resolved structure of cetyltrimethylammonium bromide wormlike micelles through the shear banding transition. J. Rheol., 53:727–756, 2009.

[15] J.M. Adams, S.M. Fielding, and P.D. Olmsted. The interplay between boundary conditions and flow geometries in shear banding: hysteresis, band configurations and surface transitions. J. Non-Newtonian Fluid Mech., 151:101–118, 2008.

[16] R. G. Larson. Constitutive Equations for Polymer Melts and Solutions. Butterworths Series in Chemical Engineering, ed. H. Brenner. Butterworths, Boston, 1988.

[17] R.K. Prud'homme and G.G. Warr. Elongational flow of solutions of rodlike micelles. Langmuir, 10:3419–3426, 1994.

[18] L.M. Walker, P. Moldenares, and J.-F. Berret. Macroscopic response of wormlike micelles in elongational flow. Langmuir, 12:6309–6314, 1996.

[19] L. Zhou, L.P. Cook, and G.H. McKinley. Probing shear-banding transition of a model of entangled wormlike micellar solutions using large amplitude oscillatory shearing (LAOS) deformation. J. Non-Newtonian Fluid Mech., to appear, 2010.

[20] M. Cromer, L.P. Cook, and G.H. McKinley. Extensional flow of wormlike micellar solutions. Chem. Eng. Science, 64:4588–4596, 2009.

[21] M. Cromer, L.P. Cook, and G.H. McKinley. Pressure-driven flow of wormlike micellar solutions in rectilinear microchannels. J. Non-Newtonian Fluid Mech., doi:10.1016/j.jnnfm.2010.11.007, 2010.

[22] C. Masselon, A. Colin, and P.D. Olmsted. Influence of boundary conditions and confinement on non local effects in flows of wormlike micellar systems. Physical Review E, 81:021502, 2010.

[23] J.Y. Lee, X.-F. Yuan, G.G. Fuller, and N.E. Hudson. Investigation of shear-banding structure in wormlike micellar solution by point-wise flow-induced birefringence measurements. J. Rheol., 49:537–550, 2005.

[24] S. Lerouge, M. Argentina, and J.P. Decruppe. Interface instability in shear-banding flow. Phys. Rev. Lett., 96:088301, 2006.

[25] M.A. Fardin, D. Lopez, J. Croso, G. Grégoire, O. Cardoso, G.H. McKinley, and S. Lerouge. Elastic turbulence in shear banding wormlike micelles. Phys. Rev. Lett., 104:178303, 2010.

[26] M. M. Britton and P. T. Callaghan. Shear banding instability in wormlike micellar solutions. Eur. Phys. Journal, B7:237–249, 1999.

[27] S.M. Fielding. Vorticity structuring and velocity rolls triggered by gradient shear bands. Phys. Rev. Lett., 76:016311, 2007.

[28] S.M. Fielding. Viscoelastic Taylor-Couette instability of shear banded flow. Phys. Rev. Lett., 104:198303, 2010.

[29] T. Yamamoto, T. Hashimoto, and A. Yamashita. Flow analysis for wormlike micellar solutions in an axisymmetric capillary channel. Rheol. Acta., 34:963–974, 2008.

[30] P. Nghe, S.M. Fielding, P. Tabeling, and A. Ajdari. Interfacially driven instability in the microchannel flow of a shear banding fluid. Phys. Rev. Letters, 104:248303, 2010.

[31] H.B. Squire. On the stability of three dimensional distribution of viscous fluid between parallel walls. Proc. R. Soc. London Ser. A, 142:621–628, 1933.

[32] M. Minale and G. Astarita. Ice streams in Antarctica: transverse instability of gravity driven flow. J. Non-Newtonian Fluid Mech., 62:155–174, 1996.

[33] F.J. Lockett. On Squire's theorem for viscoelastic fluids. J. Eng. Sci., 7:337–349, 1969.

[34] L. Blonce. Linear stability of Giesekus fluid in Poiseuille flow. Mech. Research Comm., 24:223–228, 1997.

[35] K.C. Porteous and M.M. Denn. Linear stability of plane Poiseuille flow of viscoelastic fluids. J. Rheol., 16:295–308, 1972.

[36] R. Sureshkumar and A.N. Beris. Linear stability analysis of viscoelastic Poiseuille flow using an Arnoldi-based orthogonalization algorithm. J. Non-Newtonian Fluid Mech., 56:151–182, 1995.

[37] R. Sureshkumar and A.N. Beris. Effect of artificial stress diffusivity on the stability of numerical calculations and the flow dynamics of time-dependent viscoelastic flows. J. Non-Newtonian Fluid Mech., 60:53–80, 1995.

[38] H.J. Wilson and Y. Renardy M. Renardy. Structure of the spectrum in zero Reynolds number shear flow of the UCM and Oldroyd-B liquids. J. Non-Newronian Fluid Mech., 80:251–268, 1999.

[39] T. C. Ho and M. M. Denn. Stability of plane poiseuille flow of a highly elastic liquid. J. Non-Newtonian Fluid Mech., 3:179–195, 1977.

[40] A.M. Grillet, A.C.B. Bogaerds, G.W.M. Peters, and F.P.T. Peters. Stability analysis of constitutive equations for polymer melts in viscometric flows. J. Non-Newtonian Fluid Mech., 103:221–250, 2002.

[41] H. J. Wilson and J. M. Rallison. Instability of channel flow of a shear-thinning White-Metzner fluid. J. Non-Newtonian Fluid Mech., 87:75–96, 1999.

[42] S.M. Fielding and H.J. Wilson. Shear banding and interfacial instability in planar Poiseuille flow. J. Non-Newtonian Fluid Mech., 165:196–202, 2010.

[43] S.A. Orszag. Accurate solution of the Orr-Sommerfeld stability equation. J. Fluid Mech., 50:689–703, 1971.

[44] A.N. Morozov and W. van Saarloos. Subcritical finite-amplitude solutions for plane Couette flow of viscoelastic fluids. Phys. Rev. Lett., 95:024501, 2005.

[45] H. J. Wilson and J. M. Rallison. Instability of channel flows of elastic liquids having continuously stratified properties. J. Non-Newtonian Fluid Mech., 85:293–298, 1999.

[46] C.J. Pipe, N.J. Kim, P.A. Vasquez, L.P. Cook, and G.H. McKinley. Wormlike micellar solutions II: Comparison between experimental data and scission model predictions. J. Rheol., 54:881–913, 2010.

[47] C.J. Pipe. Private communication.

[48] W.B. Black and M.D. Graham. Slip, concentration fluctuations, and flow instability in sheared polymer solutions. Macromolecules, 34:5731–5733, 2001.

[49] V.G. Mavrantzas and A.N. Beris. Theoretical study of wall effects on rheology of dilute polymer solutions. J. Rheol., 36:175–213, 1992.

[50] A.V. Bhave, R.C. Armstrong, and R.A. Brown. Kinetic theory and rheology of dilute, non-homogeneous polymer solutions. J. Chem. Phys., 95:2988–3000, 1991.

[51] H.J. Wilson, and S.M. Fielding. Linear instability of planar shear banded flow of both diffusive and non-diffusive Johnson-Segalman fluids. J. Non-Newtonian Fluid Mech., 138:181–196, 2006.

[52] A.F. Méndez-Sánchez, M.R. López-González, V.H. Rolón-Garrido, J. Pérez-González, and L. de Vargas. Instabilities of micellar systems under homogeneous and non-homogeneous flow conditions. Rheol. Acta, 42:56–63, 2003.

[53] B.M. Marín-Santibáñez, J. Pérez-González, L. de Vargas, J.P. De-Cruppe, and G. Huelsz. Visualization of shear banding and entry poiseuille flow oscillations in a micellar aqueous solution. J. Non-Newtonian Fluid Mech., 157:117–125, 2009.

[54] D.A. Goussis and A.J. Pearlstein. Removal of infinite eigenvalues in the generalized matrix eigenvalue problem. J. Comput. Phys., 84:242–246, 1989.

[55] C. Canuto, Y. M. Hussaini, A. Quarteroni, and T. A. Zang. Spectral Methods in Fluid Dynamics. Springer-Verlag, 1987.

[56] J.-P. Berrut and L.N. Trefethen. Barycentric Lagrange interpolation. SIAM Review, 46:501–517, 2004.

[57] S. Lerouge, M.A. Fardin, M. Argentina, G. Gregoire, and O. Cardoso. Interface dynamics in shear-banding flow of giant micelles. Soft Matter, 4:1808, 2008.

[58] M.A. Fardin, B. Lasne, O. Cardoso, G. Grégoire, M. Argentina, J.P. Decruppe, and S. Lerouge. Taylor-like vortices in shear-banding flow of giant micelles. Phys. Rev. Lett., 103:028302, 2009.